

---

# Deep Residual Mixture Models

---

**Perttu Hämmäläinen**  
 Aalto University  
 perttu.hamalainen@aalto.fi

**Arno Solin**  
 Aalto University  
 arno.solin@aalto.fi

## Abstract

We propose Deep Residual Mixture Models (DRMMs) which share the many desirable properties of Gaussian Mixture Models (GMMs), but with a crucial benefit: The modeling capacity of a DRMM can grow exponentially with depth, while the number of model parameters only grows quadratically. DRMMs allow for extremely flexible conditional sampling, as the conditioning variables can be freely selected without re-training the model, and it is easy to combine the sampling with priors and (in)equality constraints. DRMMs should be applicable where GMMs are traditionally used, but as demonstrated in our experiments, DRMMs scale better to complex, high-dimensional data. We demonstrate the approach in constrained multi-limb inverse kinematics and image completion.

## 1 Introduction

Gaussian Mixture Models (GMMs, *e.g.*, [1, 2]) are a classic machine learning tool with many desirable properties: They allow querying probability densities for unseen data points, computing conditional expectations, and drawing conditional samples. Furthermore, GMMs allow imputative learning, *i.e.*, the conditioning variables can be freely selected without retraining. Similarly, semi-supervised learning is straightforward, as any combination of variables can be considered unknown for each training data vector. On top of all this, GMMs afford simple geometric explanations and visualization. In principle, this makes GMMs the ideal generative model despite their age, as more modern models like Variational Autoencoders [3], Generative Adversarial Networks [4], and flow-based models [5, 6] only implement a subset of the above-mentioned features.

In practice, though, GMMs have a major drawback: They do not scale well to complex, high-dimensional data. In terms of runtime cost, this can be solved using a tree (a hierarchy) of GMMs, but the memory required grows exponentially with tree depth. To solve this problem, we propose the Deep Residual Mixture Model (DRMM), a novel architecture that allows stacking mixture model layers so that modeling capacity can *grow exponentially with depth*, while the number of model *parameters only grows quadratically*—agreeing with recent advances in showing deeper models provide more efficient approximations (*i.e.*, with fewer parameters) than shallower ones [7, 8]. Fig. 1 illustrates the effect of depth on DRMMs in a Swiss roll and Sierpinski fractal modeling task. Although the exponential growth observed in the Sierpinski case is not guaranteed for all data, our experiments (Sec. 4.3) indicate that DRMMs typically provide much better sample quality than a GMM with the same number of model parameters.

The contributions of this paper are as follows: First, we introduce the DRMM, a novel generative model that leverages the benefits of both classic GMMs and modern deep architectures. The novelty of DRMM is in the residual connections and latent variable augmentation that allow for a simple ancestral sampling approach and highly flexible conditioning of samples on both equalities and inequalities, without retraining the model (see Figs. 1 and 2). Second, we demonstrate our approach in image completion and constrained inverse kinematics (IK). In the latter, we sample the joint angles of a skeletal human body model given both end-effector target positions and inequality constraints (*e.g.*, “reach the target with your hand, while keeping your feet at given locations, and head lower

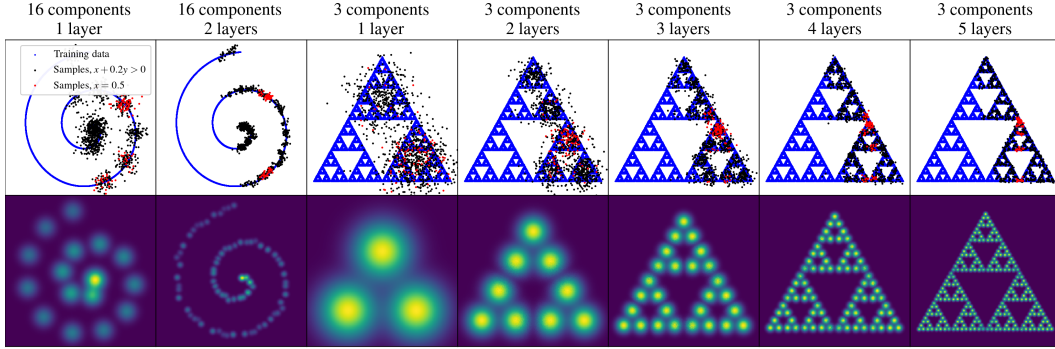


Figure 1: DRMM samples and probability density estimates with 2D training data. Samples can be easily conditioned with both equalities (red,  $x = 0.5$ ) and inequalities (black,  $x + 0.2y > 0$ ). DRMM capacity can grow exponentially with depth, exploiting data self-similarity: The Sierpinski triangle model has 3 mixture components per layer, and a  $L$ -layer DRMM models  $3^L$  density modes.

than 1.0 m”). This would be a challenging task for other generative models, but a DRMM can do the inference just by using random skeletal configurations as the training data. Uniquely, our trained IK model allows adding and removing goals and constraints without re-training, which is important for enabling an interactive human-in-the-loop workflow, *e.g.*, for computer animation.

## 2 Background and Related Work

We draw from the vast literature of deep, residual, and mixture models. As illustrated in Fig. 2 and detailed in Sects. 3 and 3.2, a characterizing feature of our DRMM architecture is that the output of each layer is a combination of a stochastic latent variable and a modeling residual. The DRMM reduces to Residual Vector Quantization (RVQ, [9, 10]), if each layer only outputs the residual and the latent variable is made deterministic by assigning each input to the most probable mixture component. RVQ is a classic data compression method, predominantly known in signal processing. However, RVQ does not allow sampling, as it stores no information of which encodings are valid ones. Through the vector quantization analogue, the DRMM is also related to VQ-VAE models [11] which apply vector quantization on the embeddings generated by convolutional encoder networks (see also [12, 13]). Many earlier approaches have utilized categorical representations with autoencoder architectures and established ways to backpropagate through samples [14, 15]. The main difference to our architecture is that we *do not* utilize a convnet encoder, which allows us to condition the encodings with any number or combination of known variables.

The DRMM has similar dimensionality-growing skip connections as DenseNets [16], but the connections are probabilistic and pass through the residual computation. DenseNets are inspired by the classic cascade-correlation networks [17] which are trained layer-wise similar to DRMMs, each added layer concatenating its input with a new latent variable. DRMMs could be considered a probabilistic generative version of cascade correlation networks. Inequality constraints in cascade correlation networks have been considered in [18], where the conditioning is implemented as a penalty term and the sampling done via MCMC, which can be computationally costly.

Extensions to plain Gaussian mixtures feature, for example, residual k-means [19] that also increases intrinsic dimensionality, but using trees. Our model can be considered similar, with a layer per tree level, but with weight-sharing between subtrees to avoid the storage cost growing exponentially with depth. There are also hierarchical Gaussian mixture models (*e.g.*, [20]), that do not, however, feature residual connections. Each layer of a DRMM can also be considered a simple autoencoder. Traditional autoencoder stacks utilize successive per-layer encoding and decoding steps during pre-training. Yet, the decoders are discarded and a final output layer still needs to be trained, and they are also only trained on predictors in the classifier case [21].

For deep generative modeling, several approaches have been proposed during the past decade. Energy-based models such as Deep Boltzmann Machines (DBMs, [22]) can utilize greedy layer-by-layer training—same as DRMMs—but in a variational approximation framework. Flow-based models [5, 6, 23, 24] are similar to DRMMs in that layers are invertible and each layer outputs

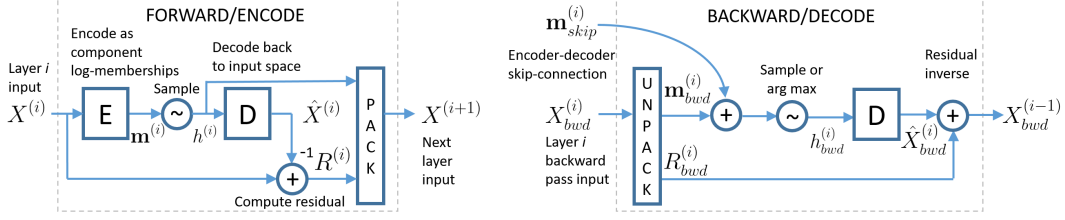


Figure 2: DRMM architecture, showing the forward and backward passes over a single layer. Each layer is a mixture model that encodes the input  $X$  as mixture component membership logits  $\mathbf{m}$ , samples a component index  $h$ , and passes it and the modeling residual  $R$  to the next layer.

an incrementally ‘whitened’ distribution that is easier to sample. The benefit of DRMMs over these models as well as Variational Autoencoders [3] and Generative Adversarial Networks [4] is the capability of conditioning a trained model with arbitrary variable combinations and inequality constraints, which comes at no additional cost and requires no modifications to the training.

### 3 Deep Residual Mixture Models

As illustrated in Fig. 2, each DRMM layer is a mixture model that encodes the input  $X$  as a vector of mixture component membership log-probabilities  $\mathbf{m}$  and samples a categorical stochastic latent variable  $h \sim \text{softmax}(\mathbf{m})$ . The next layer models the joint distribution of the latent and the modeling residual  $R$ . This way, each layer progressively extracts more information from the input data. In Fig. 2, we denote layer indices by superscripts, but we drop them in the following for brevity. Discussing the operation of a single layer is enough, as each layer is trained independently, and the full probability density of the deep model is given by the last layer (see Fig. 1 for examples).

The inputs and residuals of each layer are composed of multiple *input streams*, which we denote as tuples of vectors  $X = [\mathbf{x}_1, \mathbf{x}_2, \dots]$  and  $R = [\mathbf{r}_1, \mathbf{r}_2, \dots]$ . The vectors  $\mathbf{x}_i, \mathbf{r}_i$  of stream  $i$  represent either real-valued multivariate data or log-probability distributions over a categorical variable. The ‘pack’ operation in Fig. 2 denotes appending the residual with the latent  $h$  as a new categorical stream, encoded as the log-probability distribution  $\log \text{smooth}(\text{onehot}(h))$ . Logarithms of 0 are avoided as  $\text{smooth}(x) = (1.0 - \epsilon)x + \epsilon/K$ , with  $\epsilon = 10^{-8}$ . Stream tuple arithmetic is performed element-wise:  $R = X - \hat{X} = [\mathbf{x}_1 - \hat{\mathbf{x}}_1, \mathbf{x}_2 - \hat{\mathbf{x}}_2, \dots]$ .

#### 3.1 Computing Membership Probabilities

A key assumption we utilize is that the input streams and individual input variables are all conditionally independent given the memberships. Thus, each DRMM layer can be conceptualized as an unsupervised Naïve Bayes classifier, and memberships conditional on each stream and/or variable have simple closed-form expressions that combine multiplicatively.

We set up each layer to define a mixture probability density over an input  $X$  as:

$$p(X | \theta) \propto \sum_{k=1}^K m_k(X, \theta_k) = \sum_{k=1}^K w_k \prod_s f_{k,s}(\mathbf{x}_s | \theta_{k,s}), \quad (1)$$

where  $\theta$  denotes layer parameters,  $k$  is mixture component index,  $K$  is the number of components,  $m$  is the unnormalized membership probability of input  $X$  belonging to a mixture component,  $w_k$  is a weight or marginal probability of a component,  $s$  is input stream index, and  $f_{k,s}(\cdot)$  is the membership probability density function for component  $k$  and stream  $s$ .

We model real-valued data as a Gaussian mixture with the same isotropic covariance matrix for each component,  $\mathbf{C}_k = \sigma^2 \mathbf{I}$ . The parameters include the variance and component means,  $\theta = (\mu_1, \mu_2, \dots, \mu_K, \sigma)$ , and the component probability density function is given as  $f_k(\mathbf{x} | \theta_k) = \mathcal{N}(\mathbf{x} | \mu_k, \sigma^2)$ , or equivalently,  $\log f_k(\mathbf{x} | \theta_k) = -1/2(\|\mathbf{x}_r - \mu_{k,r}\|^2 / \sigma_r^2 + K \log \sigma_r^2)$ .

For categorical input streams, using  $\mathbf{y} = \text{softmax}(\mathbf{x})$  to get from logits to probabilities, we utilize the multinomial Naïve Bayes classifier formula  $f_k(\mathbf{y} | \theta_k) = \prod_{i=1}^N p_{k,i}^{y_i}$ , or equivalently,  $\log f_k(\mathbf{x} | \theta_k) =$

$\text{softmax}(\mathbf{x})^\top \log \mathbf{p}_k$ , where  $\mathbf{p}_k$  is a vector of ‘feature’ probabilities given class  $k$ . The parameters for component  $k$  are  $\boldsymbol{\theta}_k = \mathbf{p}_k = (p_{k,1}, p_{k,2}, \dots, p_{k,M})$ , where  $M$  is the number of input stream categories.

To prevent underflows in combining the contributions of multiple streams, we operate in the log-domain, resulting in the complete membership probability formula:

$$\begin{aligned} \log(m_k(X, \boldsymbol{\theta}_k)) = & \log w_k - \frac{1}{2} \sum_{r \in \mathcal{S}_{\text{real}}} (\|\mathbf{x}_r - \boldsymbol{\mu}_{k,r}\|^2 / \sigma_r^2 + K \log \sigma_r^2) \\ & + \sum_{c \in \mathcal{S}_{\text{cat}}} \text{softmax}(\mathbf{x}_c)^\top \log \mathbf{p}_{k,c} + \rho \sum_{l \in \mathcal{S}_{\text{latent}}} \text{softmax}(\mathbf{x}_l)^\top \log \mathbf{p}_{k,l}, \end{aligned} \quad (2)$$

where  $\mathcal{S}_{\text{real}}$  and  $\mathcal{S}_{\text{cat}}$  are the sets of real-valued and categorical input streams, except for the categorical input streams corresponding to the latent variables of previous layers, denoted  $\mathcal{S}_{\text{latent}}$ . The parameter  $\rho$  controls sample precision, as detailed in Sec. 3.5. Intuitively, Eq. (2) is a measure of distance from the input  $X$  to the  $k^{\text{th}}$  mixture component. The measure additively combines Mahalanobis distance for real-valued streams and differential entropy for categorical streams. If input variables are unknown, one can simply omit their contributions from the dot products and the squared norm, and substitute the number of known variables for  $K$ .

Using the notation above, we can write  $\mathbf{m}$  in Fig. 2 as

$$\mathbf{m}(X, \boldsymbol{\theta}) = (\log(m_1(X, \boldsymbol{\theta}_1)), \dots, \log(m_K(X, \boldsymbol{\theta}_K))). \quad (3)$$

### 3.2 Residual Computation

A key feature of the DRMM is that each layer outputs both the latent variable and the residual streams  $\mathbf{r} = \mathbf{x} - \hat{\mathbf{x}}$ , where  $\hat{\mathbf{x}}$  equals the  $\boldsymbol{\mu}_h$  or  $\mathbf{p}_h$  of the sampled mixture component. The rationale for this is two-fold: First, it ensures that no information is lost despite the limited accuracy of the latent encoding, which allows layers to be (approximately) inverted as in Fig. 2 and later layers to progressively extract more structure. Second, as all  $K$  component means of a layer are mapped to the origin of the residual space, this produces a one-to- $K$  mapping from the next layer’s input space to the previous layer (see Fig. 3). *This allows layer  $i$  to model  $K^i$  probability density modes with a single mixture component.* The portion of valid modes depends on data self-similarity. If the neighborhoods of each component mean align perfectly, as with the Sierpinski fractal, each  $\mathbf{r}$  maps to  $K$  valid  $\mathbf{x}$ .

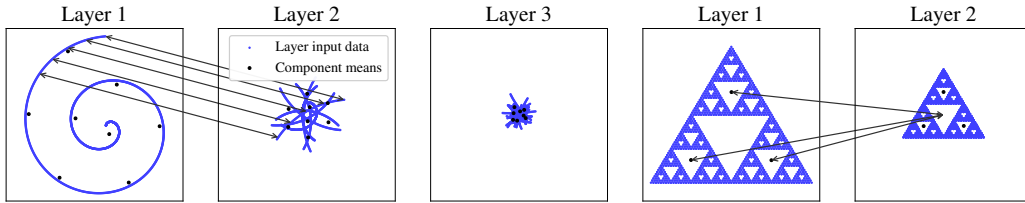


Figure 3: Visualizing the residual computation in the examples in Fig. 1. The first DRMM layer sees the original input data, while other layers see the residual of the previous layer. The arrows show examples of how layer inputs map to residuals and back.

### 3.3 Sampling

Sampling from a DRMM is simple: Pass data through the layers, sample the latents and sum the  $\hat{\mathbf{x}}$  of each layer. Optionally, one may also add Gaussian noise using the last layer’s  $\sigma^2$ , but according to our experience, deep models give better results without it. The noise is added in Fig. 1 to make the samples consistent with the density plots.

### 3.4 Training with Expectation Maximization

A common way to train mixture models (and semi-/unsupervised Naïve Bayes) is through Expectation Maximization (EM) [25]. This is set up as an iteration of two steps, which we perform once for each training data minibatch and independently for each layer:

**E-step:** Estimate the membership probabilities given input data and parameters.

**M-step:** Maximize the probability of data by optimizing parameters while keeping the membership probabilities fixed.

In the unsupervised Naïve Bayes interpretation, the M-step corresponds to training the classifier by using the E-step results as the ground-truth class labels. In the E-step, we compute the membership logits using Eq. (3). Denoting these as  $\hat{\mathbf{m}}$  and using the most probable memberships as the ground truth, we can implement the M-step as an Adam [26] optimization step on the standard cross-entropy classification loss averaged over  $N$  minibatch samples:

$$\mathcal{L}_{\theta} = \frac{1}{N} \sum_{i=1}^N \text{onehot}(\arg \max(\hat{\mathbf{m}}_i))^{\top} \mathbf{m}(X_i, \theta), \quad (4)$$

where the  $\arg \max$  is over the elements of  $\hat{\mathbf{m}}_i$ .

### 3.5 Regularizing the Training: Modified E-step

The  $\rho$  parameter in Eq. (2) allows one to adjust the tradeoff between sample precision and recall, as shown in Fig. 4 for  $\rho = 0, 0.5, 1$ . However, it is difficult to get both high recall and high precision. We solve the problem by modifying the E-step  $\rho$ . The M-step and inference always use  $\rho = 1$ . With E-step  $\rho = 0$ , the ‘ground truth’ class labels  $\hat{\mathbf{m}}$  prioritize minimizing the modeling residual of the first layer’s input data, disregarding the latents of previous layers and thus minimizing circular dependency of the ‘ground truth’ on the learned  $\theta$ . As shown in Fig. 4, this gives good recall and fairly high precision. Precision can be further increased by increasing  $\rho$  after initial training. To further minimize circular dependencies, we also omit the marginal probabilities  $w_k$  from the E-step, similar to the common practice of pretraining GMMs with  $K$ -means clustering.

Fitting mixture models with EM is also prone to ‘orphan’ components that get assigned no data. We prevent this with a regularization loss that penalizes the distance of each centroid from the sample closest to it:  $1/K \sum_k \alpha \max_i \log(m_k(X_i | \theta_k))|_{\rho=0, w_k=0}$ , with  $\alpha = 0.01$ .

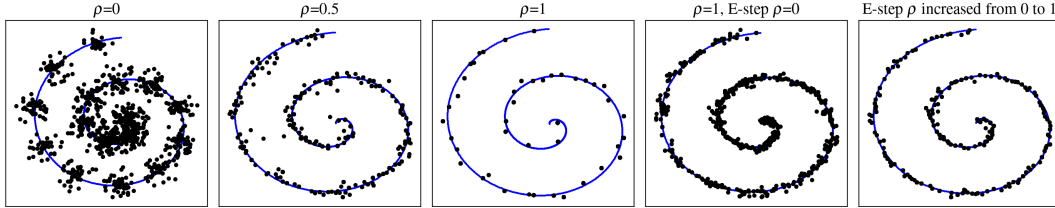


Figure 4: Effect of the  $\rho$  parameter on DRMM sample quality. The model has 3 layers and 16 components per layer. The best combination of precision and recall is obtained with the modified E-step,  $\rho$  gradually increased from 0 during training.

### 3.6 Conditioning and Constraining the Sampling

Conditioning and constraining samples can be thought as multiplying the sampling PDF with a prior. We consider Gaussian priors and linear inequality and equality constraints of type  $\mathbf{a}^{\top} \mathbf{x} + b > 0$  and  $\mathbf{a}^{\top} \mathbf{x} + b = 0$ . Such an inequality corresponds to a prior that is zero in the half-space where the constraint is not satisfied. The equality corresponds to a prior that is zero except on a hyperplane. The DRMM makes it easy to apply constraints and priors because the simple residual computation allows the priors to be transformed to the residual space. Hence, *the priors can pass through the network along with the data* and inform each sampled latent. Substituting  $\mathbf{x} = \mathbf{r} + \hat{\mathbf{x}}$  to the linear constraint inequality, one gets the residual constraint  $\mathbf{a}_r^{\top} \mathbf{r} + b_r > 0$ , where  $\mathbf{a}_r = \mathbf{a}$ ,  $b_r = b + \mathbf{a}^{\top} \hat{\mathbf{x}}$ . For Gaussian priors, one only needs to shift the prior mean by  $-\hat{\mathbf{x}}$ , similar to each input vector.

At each layer, the priors are applied in the mixture component selection: The membership probability of a component is multiplied by the integral of the product of the prior and the component’s Gaussian PDF. Since we use isotropic covariances for the components, evaluating the integral for prior Gaussians is trivial, and linear constraints only need to be integrated in 1D along the constraint hyperplane normal. As illustrated in Fig. 1, the constraints become more accurate with depth, as the DRMM’s resolution grows and the component  $\sigma$  decreases.

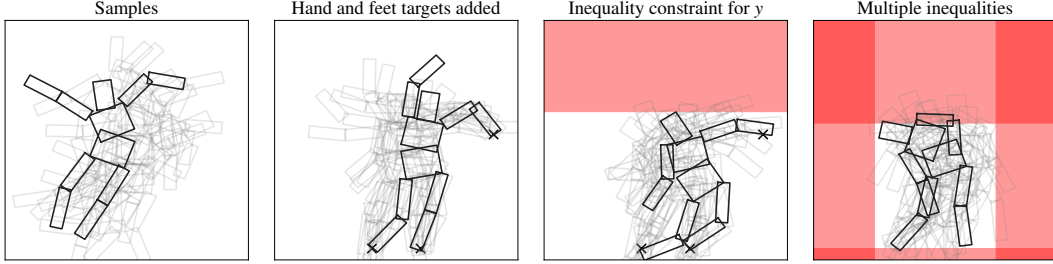


Figure 5: 10-layer DRMM samples of humanoid root position, rotation, and joint angles, conditioned on goals and inequality constraints for head, hands, and/or feet. Uniquely, our model allows using any combination of goals and constraints, after training only once on random body configurations.

### 3.7 Backward Sampling

Intuitively, each DRMM layer increases the independence of the residuals, as the residual computation removes structure modeled by the latent. Assuming independence of the last DRMM layer outputs, one can (i) batch-average the categorical latent PDFs output by the last layer to combine information from all samples in the batch, and (ii) map the combined latent distribution back to the input space via a backward pass over each layer, illustrated in Fig. 2. The backward pass inverts the residual computation  $R = X - \hat{X}$  as  $X_{bwd} = R_{bwd} + \hat{X}_{bwd}$ . The  $\hat{X}_{bwd}$  is determined by the latent  $h_{bwd}$  similar to the forward pass. One can either sample the latent to synthesize variation, or take arg max to only construct a single probable input-space sample. This allows implementing model hierarchies where a forward pass integrates information from multiple models and a backward pass samples each model (see Sec. 4.2 for an application in sampling images).

Fig. 2 also shows the encoder-decoder skip-connections that can be added to bring back detail lost in the forward pass, reminiscent of the U-net for image segmentation [27]. We use  $\mathbf{m}_{\text{skip}} = \alpha_{\text{skip}} \log(\text{batch\_average}(\text{softmax}(\mathbf{m})))$ , where  $\alpha_{\text{skip}}$  is a tuning parameter. The skip-connections are additive, as they operate on membership log-probabilities. If an encoder layer produces a uniform membership distribution or if  $\alpha_{\text{skip}} = 0$ , the skip-connection has no effect.

## 4 Experiments

We demonstrate the properties of the DRMM in constrained multi-limb inverse kinematics (IK) and image completion, and compare sample quality quantitatively against a GMM baseline. For the IK task, there are no similarly flexible models that allow for direct conditioning and inequality constraints (without augmentation, re-training, or increased computational cost). The image completion task demonstrates DRMM model hierarchies and backward sampling of high-dimensional data, but it should be noted that we do not intend to compete with purpose-built image completion/inpainting models [28–30] in terms of image quality. The value of the DRMM architecture is in its generality.

### 4.1 Constrained Inverse Kinematics

Fig. 5 demonstrates DRMM conditioned and constrained sampling in inverse kinematics, a common problem in robotics and computer animation. IK solvers output the skeletal joint angles given one or more end-effector goal positions and constraints. This is only simple for chains of two bones, and iterative optimization and/or machine learning methods are needed for more complex skeletal structures [31–33]. Typically, multiple solutions exist for each IK problem, and it would be beneficial to have a generative model that can sample alternative solutions. These solutions could be used as such, or to initialize an optimization routine.

We train a DRMM with 10 layers and 256 components per layer, using 1M random skeletal configurations of the 2D humanoid in Fig. 5. Each training data vector has 30 variables: root position and rotation, joint angles, and the world coordinates of hands, feet, top of the head, and center of mass. As illustrated in Fig. 5, the model correctly infers both root and joint parameters to approximately satisfy the goals and constraints. The figure shows random samples and the sample from a batch of 64 that best satisfies the goals and constraints. The inequality constraints are applied to hand, feet,



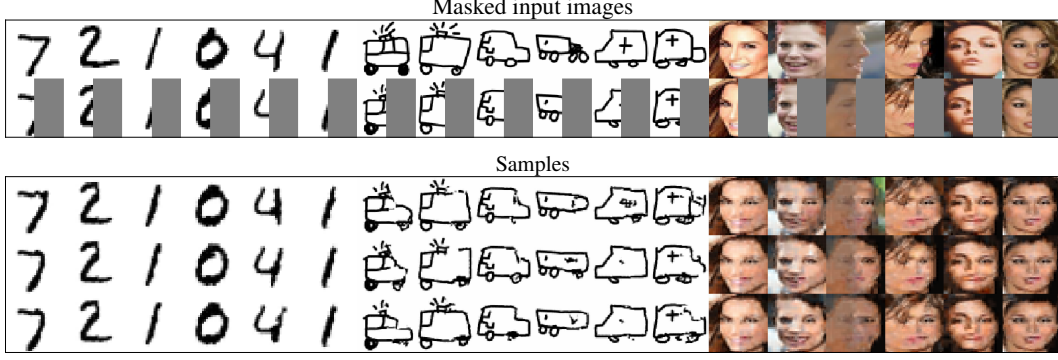


Figure 6: Image samples conditioned on known pixels of  $28 \times 28$  pixel MNIST,  $64 \times 64$  Quick, Draw! ambulance, and  $32 \times 32$  CelebA images not used in training. See the paper supplement for more.

and head coordinates. We know of no other machine learning based IK solution that allows one to add an arbitrary number of goals and constraints after only training once with random data.

## 4.2 Image Completion

To test backward sampling of high-dimensional data, we trained DRMMs on  $28 \times 28$  pixel MNIST handwritten characters [34],  $64 \times 64$  antialiased rasterizations of Quick! Draw [35] ambulance sketches, and  $32 \times 32$  cropped CelebA faces [36]. We used the full MNIST training set, 200k Quick! Draw images, and all 202k CelebA images except for 100 ones reserved for testing. Fig. 6 shows how samples can be conditioned on known (not masked) pixels, without any changes to the training. The MNIST samples are of similar quality as the reference data, and the other samples also exhibit correct structure although details are not as well defined as in the input images. As to be expected, CelebA sample quality is worse for inputs with outlier face rotations.

Motivated by the convolution hierarchies common in neural image processing, we use a hierarchy of DRMM blocks: For each block, we extract  $3 \times 3$  pixel patches with stride 2, and model the patch distributions with  $L$ -layer DRMMs that share weights. The categorical latent variable outputs of the patch DRMMs form the input image for the next block, with  $LK$  image channels and resolution halved due to the striding. The last block models its whole input without patch extraction. The MNIST, Quick! Draw, and CelebA models have 10, 28, and 28 layers, and 13.2M, 65.9M, and 86.8M parameters, respectively. More implementation details are provided in the supplementary material. We utilize the backward sampling of Sec. 3.7: The forward pass integrates the local patch information into global latent samples, and the backward pass maps the samples back to pixels. During the backward pass, we only sample the latents of the last DRMM block to ensure globally coherent samples. We sample with truncation, zeroing out component sampling probabilities below  $\alpha_t \max_k p_k$ , where  $p_k$  is the sampling probability of component  $k$ . We use  $\alpha_t = 0.02$ .

## 4.3 Quantitative Comparison to GMM

The benefits of DRMMs compared to a GMM with the same number of components are clear in Fig. 1. However, as the number of DRMM parameters grows nonlinearly with depth and component count, a question remains whether one could simply use a very large GMM with the same number of parameters. A DRMM component is defined by the scalar  $w$  and the vector  $\mu$  or  $\mathbf{p}$  of length  $D$ , where  $D$  is the layer’s input dimensionality. A layer has  $K$  components and also the scalar  $\sigma$ . Thus, a layer has  $(D + 1)K + 1 \approx DK$  parameters. Dimensionality grows as  $D = D_1 + (l - 1)K$ , where  $l$  is layer index and  $D_1$  is the first layer’s input dimensionality. Substituting this to  $DK$  and summing over  $L$  layers results in a total of  $D_1 LK + 0.5L(L - 1)K^2$  model parameters.

Fig. 7 compares DRMMs of various depths and component counts to GMMs with up to 1024 components, using F1 scores computed using the precision and recall metric of Kynkäänniemi et al. [37]. DRMMs provide better sample quality for a given total parameter count except for the simple 3D Swiss roll data—with low-dimensional data (small  $D_1$ ), a GMM gives good results and the number of DRMM parameters is dominated by the  $L(L - 1)K^2$  term. The arm IK data is from a 2D

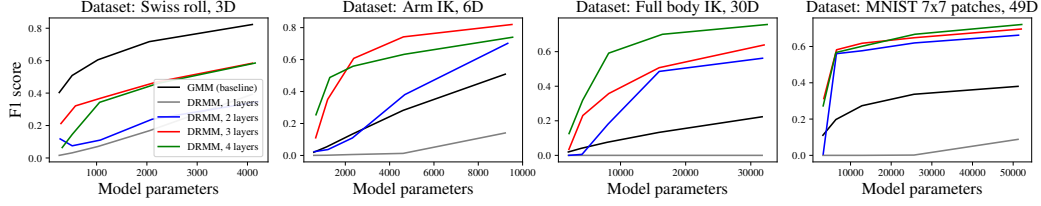


Figure 7: Benchmarking DRMM against a GMM baseline (black) in terms of sample quality. For more complex datasets, DRMM clearly beats a GMM with the same number of model parameters.

4-link arm, with 6 variables (4 angles, 2 end effector coordinates). The full-body IK data is the same as in Sec. 4.1. The MNIST patch data is motivated by the patch hierarchies used in Sec. 4.2. For a controlled comparison, the baseline GMMs use scalar covariances, *i.e.*, they are equal to single-layer DRMMs that add Gaussian noise with  $\sigma$  after sampling a mixture component.

## 5 Limitations and Future Work

The primary limitation of DRMMs is that density estimation and backward sampling require averaging over a batch of samples. The density plots of Fig. 1 and image completion of Fig. 6 use batch sizes 32 and 256, respectively. We are presently investigating whether this limitation can be lifted by quantizing all input variables and using an all-categorical DRMM where the forward pass does not sample the latents but instead propagates full discrete PDFs of the latents and residuals.

As discussed in Sec. 3.2, the expressivity of a DRMM depends on the alignment of the residuals of inputs assigned to each mixture component. Presently, the residual computation is a very simple geometric transform, and we hypothesize that there are other suitable transforms that maximize the alignment. For instance, one might learn a per-component scaling and rotation of the residuals.

Finally, we have so far only demonstrated two DRMM applications. It should be straightforward to extend the IK example to synthesizing movement sequences, *e.g.*, training a DRMM with motion capture data, and allowing an animator to specify complete or partial target poses at desired times, possibly with additional constraints such as dodging below and obstacle. It should also be possible to model text and infer missing words or sentences similar to the image completion task, but using 1D arrays of categorical (tokenized) input data instead of 2D arrays of pixel colors.

## 6 Conclusion

We have presented the DRMM, a generative model that combines the benefits of classic GMMs with the (best-case) exponential capacity growth of modern deep architectures. We contribute through the novel residual connection and latent variable augmentation architecture, which allows extremely flexible sample conditioning and constraining without re-training the model. According to our experiments, one can train a DRMM without *a priori* knowledge of multivariate relations, and then *predict anything from anything*. It should also be possible to combine DRMMs with neural architectures that utilize mixture models or vector quantization as a building block [11, 38], substituting a DRMM as a more scalable and versatile alternative.

We find it intriguing that the complex learning ability of DRMMs emerges from stacking multiple elementary layers without backpropagation between layers, each layer learning independently. It is surprising that the simple recursive approach allows (i) passing constraints and priors through the network along with the data, and (ii) mapping any combination of known variables, constraints, and priors to a latent representation that allows inferences of unknown variables, *e.g.*, image pixels. This is interesting from the point of view of biologically plausible, self-organizing artificial intelligence.

The supplementary material provides additional results and implementation details. Code, pretrained models, and video examples can be found at <https://github.com/PerttuHamalainen/DRMM>.



## Broader Impact

Considering the broader themes in ML and AI research, we contribute to *interactive AI*: The flexible sample conditioning and constraining of our DRMM architecture provides new tools for interactive human-in-the-loop exploration of model outputs. For example, it should be possible to extend our IK example into a full-blown animation application where an animator defines goals and constraints for an animated character—*e.g.*, start pose, goal pose, movements, or obstacles to avoid—and a DRMM then suggests possible movement trajectories. This would be an example of Mixed-Initiative Interaction [39] and Mixed-Initiative Co-Creativity [40], where a human designer and an intelligent system augment each other, instead of an AI tool simply taking over and replacing human workers. This supports the goal of non-destructive integration of AI technology with society and economy.

Another theme that our work has potential to contribute is *explainable and interpretable AI* [41–43]. The DRMM architecture is motivated by simple geometric intuitions, and it is easy to visualize the mixture components and the modeling residuals of each layer, at least for real-valued inputs (*e.g.*, Fig. 3). Each DRMM layer also makes a simple classification decision, essentially based on template matching: Which of the mixture component centroids is the input vector closest to? This might make it easier to visualize and explain the chain of decisions that produced a particular inference, much like inspecting the decisions made by a decision tree. However, this is currently only speculation, as we have not yet investigated any DRMM applications where explainability would be crucial.

Considering the dialogue between neuroscience, cognitive science, and AI research, our results provide new evidence that complex learning is possible through combining simple self-organizing layers without backpropagation of gradients through a network. This is valuable because no biological basis for backpropagation is known, although the brain may be able to approximate it [44]. Previously, the cascade-correlation network architecture [17] has been used to model cognitive development [45], and the DRMM can be considered a probabilistic generative version of cascade-correlation networks, with similar layer-wise training and dimensionality-growing latent variable augmentation.

Beyond the above, our work shares the general societal and ethical concerns of all AI & ML research; we propose a new general-purpose model architecture that could be applied in a wide range of contexts.

## Acknowledgments and Disclosure of Funding

This work has been supported by Academy of Finland grant 299358 and the computing resources provided by Aalto University’s Triton computing cluster.

## References

- [1] Christopher M Bishop. *Pattern Recognition and Machine Learning*. Springer, 2006.
- [2] Marc Peter Deisenroth, A Aldo Faisal, and Cheng Soon Ong. *Mathematics for Machine Learning*. Cambridge University Press, 2020.
- [3] Diederik P. Kingma and Max Welling. Auto-encoding variational Bayes. In *International Conference on Learning Representations (ICLR)*, 2014.
- [4] Ian Goodfellow, Jean Pouget-Abadie, Mehdi Mirza, Bing Xu, David Warde-Farley, Sherjil Ozair, Aaron Courville, and Yoshua Bengio. Generative adversarial nets. In *Advances in Neural Information Processing Systems 27 (NIPS)*, pages 2672–2680. Curran Associates, Inc., 2014.
- [5] Laurent Dinh, Jascha Sohl-Dickstein, and Samy Bengio. NICE: Non-linear independent components estimation. In *International Conference on Learning Representations (ICLR)*, 2015.
- [6] Danilo Rezende and Shakir Mohamed. Variational inference with normalizing flows. In *Proceedings of the 32nd International Conference on Machine Learning (ICML)*, volume 37 of *Proceedings of Machine Learning Research*, pages 1530–1538. PMLR, 2015.
- [7] Ben Poole, Subhaneil Lahiri, Maithra Raghu, Jascha Sohl-Dickstein, and Surya Ganguli. Exponential expressivity in deep neural networks through transient chaos. In *Advances in Neural Information Processing Systems 29 (NIPS)*, pages 3360–3368. Curran Associates, Inc., 2016.

- [8] David Rolnick and Max Tegmark. The power of deeper networks for expressing natural functions. In *International Conference on Learning Representations (ICLR)*, 2018.
- [9] Biing-Hwang Juang and A Gray. Multiple stage vector quantization for speech coding. In *IEEE International Conference on Acoustics, Speech, and Signal Processing (ICASSP)*, volume 7, pages 597–600. IEEE, 1982.
- [10] Faouzi Kossentini, Mark JT Smith, and Christopher F Barnes. Image coding using entropy-constrained residual vector quantization. *IEEE Transactions on Image Processing*, 4(10):1349–1357, 1995.
- [11] Aaron van den Oord, Oriol Vinyals, and Koray Kavukcuoglu. Neural discrete representation learning. In *Advances in Neural Information Processing Systems 30 (NIPS)*, pages 6306–6315. Curran Associates, Inc., 2017.
- [12] Cristina Gărbacea, Aäron van den Oord, Yazhe Li, Felicia SC Lim, Alejandro Luebs, Oriol Vinyals, and Thomas C Walters. Low bit-rate speech coding with vq-vae and a wavenet decoder. In *IEEE International Conference on Acoustics, Speech, and Signal Processing (ICASSP)*, pages 735–739. IEEE, 2019.
- [13] Ali Razavi, Aaron van den Oord, and Oriol Vinyals. Generating diverse high-fidelity images with VQ-VAE-2. In *Advances in Neural Information Processing Systems 32 (NeurIPS)*, pages 14837–14847. Curran Associates, Inc., 2019.
- [14] Chris J Maddison, Andriy Mnih, and Yee Whye Teh. The concrete distribution: A continuous relaxation of discrete random variables. In *International Conference on Learning Representations (ICLR)*, 2017.
- [15] Eric Jang, Shixiang Gu, and Ben Poole. Categorical reparameterization with Gumbel-Softmax. In *International Conference on Learning Representations (ICLR)*, 2017.
- [16] Gao Huang, Zhuang Liu, Laurens Van Der Maaten, and Kilian Q Weinberger. Densely connected convolutional networks. In *Proceedings of the IEEE Conference on Computer Vision and Pattern Recognition (CVPR)*, pages 4700–4708, 2017.
- [17] Scott E Fahlman and Christian Lebiere. The cascade-correlation learning architecture. In *Advances in Neural Information Processing Systems 2 (NIPS)*, pages 524–532. Morgan-Kaufmann, 1990.
- [18] Ardavan Salehi Nobandegani and Thomas R Shultz. Example generation under constraints using cascade correlation neural nets. In *40th Annual Cognitive Science Society Meeting (CogSci)*, pages 2388–2393, 2018.
- [19] Jiangbo Yuan and Xiuwen Liu. Transform residual k-means trees for scalable clustering. In *IEEE 13th International Conference on Data Mining Workshops*, pages 489–496. IEEE, 2013.
- [20] Vincent Garcia, Frank Nielsen, and Richard Nock. Hierarchical gaussian mixture model. In *IEEE International Conference on Acoustics, Speech, and Signal Processing (ICASSP)*, pages 4070–4073, 2010.
- [21] Pascal Vincent, Hugo Larochelle, Isabelle Lajoie, Yoshua Bengio, and Pierre-Antoine Manzagol. Stacked denoising autoencoders: Learning useful representations in a deep network with a local denoising criterion. *Journal of Machine Learning Research*, 11(110):3371–3408, 2010.
- [22] Ruslan Salakhutdinov and Geoffrey Hinton. Deep Boltzmann machines. In *Proceedings of the Twelfth International Conference on Artificial Intelligence and Statistics*, volume 5 of *Proceedings of Machine Learning Research*, pages 448–455. PMLR, 2009.
- [23] Laurent Dinh, Jascha Sohl-Dickstein, and Samy Bengio. Density estimation using real NVP. In *International Conference on Learning Representations (ICLR)*, 2017.
- [24] Durk P Kingma and Prafulla Dhariwal. Glow: Generative flow with invertible  $1 \times 1$  convolutions. In *Advances in Neural Information Processing Systems 31 (NeurIPS)*, pages 10215–10224. Curran Associates, Inc., 2018.
- [25] Arthur P Dempster, Nan M Laird, and Donald B Rubin. Maximum likelihood from incomplete data via the EM algorithm. *Journal of the Royal Statistical Society: Series B (Methodological)*, 39(1):1–22, 1977.
- [26] Diederik P Kingma and Jimmy Ba. Adam: A method for stochastic optimization. In *International Conference on Learning Representations (ICLR)*, 2015.
- [27] Olaf Ronneberger, Philipp Fischer, and Thomas Brox. U-net: Convolutional networks for biomedical image segmentation. In *International Conference on Medical Image Computing and Computer-assisted Intervention*, pages 234–241. Springer, 2015.

- [28] Aäron Van Den Oord, Nal Kalchbrenner, and Koray Kavukcuoglu. Pixel recurrent neural networks. In *Proceedings of the 33rd International Conference on Machine Learning-Volume 48*, pages 1747–1756, 2016.
- [29] Chao Yang, Xin Lu, Zhe Lin, Eli Shechtman, Oliver Wang, and Hao Li. High-resolution image inpainting using multi-scale neural patch synthesis. In *Proceedings of the IEEE Conference on Computer Vision and Pattern Recognition (CVPR)*, pages 6721–6729, 2017.
- [30] Jiahui Yu, Zhe Lin, Jimei Yang, Xiaohui Shen, Xin Lu, and Thomas S Huang. Generative image inpainting with contextual attention. In *Proceedings of the IEEE Conference on Computer Vision and Pattern Recognition (CVPR)*, pages 5505–5514, 2018.
- [31] Keith Grochow, Steven L Martin, Aaron Hertzmann, and Zoran Popović. Style-based inverse kinematics. *ACM Transactions on Graphics*, 23(3):522–531, 2004.
- [32] Andreas Aristidou and Joan Lasenby. Inverse kinematics: A review of existing techniques and introduction of a new fast iterative solver. Technical report, 2009. CUED/F-INFENG/TR-632, Department of Engineering, University of Cambridge.
- [33] Raşit Köker. A genetic algorithm approach to a neural-network-based inverse kinematics solution of robotic manipulators based on error minimization. *Information Sciences*, 222:528–543, 2013.
- [34] Yann LeCun, Léon Bottou, Yoshua Bengio, and Patrick Haffner. Gradient-based learning applied to document recognition. *Proceedings of the IEEE*, 86(11):2278–2324, 1998.
- [35] David Ha and Douglas Eck. A neural representation of sketch drawings. In *International Conference on Learning Representations (ICLR)*, 2018.
- [36] Ziwei Liu, Ping Luo, Xiaogang Wang, and Xiaoou Tang. Deep learning face attributes in the wild. In *Proceedings of International Conference on Computer Vision (ICCV)*, December 2015.
- [37] Tuomas Kynkäänniemi, Tero Karras, Samuli Laine, Jaakko Lehtinen, and Timo Aila. Improved precision and recall metric for assessing generative models. In *Advances in Neural Information Processing Systems 32 (NeurIPS)*, pages 3929–3938. Curran Associates, Inc., 2019.
- [38] ZongYuan Ge, Chris McCool, Conrad Sanderson, and Peter Corke. Modelling local deep convolutional neural network features to improve fine-grained image classification. In *IEEE International Conference on Image Processing (ICIP)*, pages 4112–4116. IEEE, 2015.
- [39] J. E. Allen, C. I. Guinn, and E. Horvitz. Mixed-initiative interaction. *IEEE Intelligent Systems and Their Applications*, 14(5):14–23, 1999.
- [40] Georgios N Yannakakis, Antonios Liapis, and Constantine Alexopoulos. Mixed-initiative co-creativity. In *Proceedings of the 9th International Conference on the Foundations of Digital Games*. Foundations of Digital Games, 2014.
- [41] P Voosen. How AI detectives are cracking open the black box of deep learning. *Science*, July 2017.
- [42] W James Murdoch, Chandan Singh, Karl Kumbier, Reza Abbasi-Asl, and Bin Yu. Definitions, methods, and applications in interpretable machine learning. *Proceedings of the National Academy of Sciences*, 116(44):22071–22080, 2019.
- [43] Danding Wang, Qian Yang, Ashraf Abdul, and Brian Y Lim. Designing theory-driven user-centric explainable ai. In *Proceedings of the 2019 CHI Conference on Human Factors in Computing Systems*, pages 1–15, 2019.
- [44] Timothy P Lillicrap, Adam Santoro, Luke Marris, Colin J Akerman, and Geoffrey Hinton. Backpropagation and the brain. *Nature Reviews Neuroscience*, pages 1–12, 2020.
- [45] Thomas R Shultz. Constructive artificial neural-network models for cognitive development. *New Perspectives on Human Development*, pages 15–26, 2017.

---

# Supplementary Material for Deep Residual Mixture Models

---

This supplementary document is organized as follows. App. A presents additional results, App. B tackles questions related to sampling bias, and implementation details are provided in App. C.

## A Additional Results

### A.1 Image Completion

Fig. 8 shows more conditional image samples. Fig. 9 illustrates how the encoder–decoder skip-connections improve sample quality.

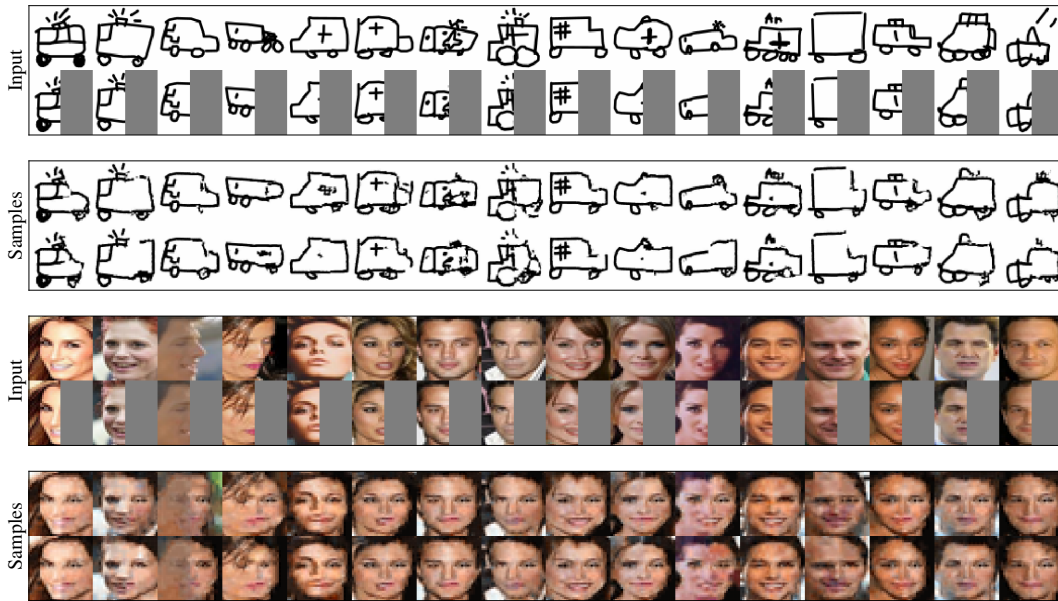


Figure 8: Image samples conditional on known (not masked) pixels, augmenting Fig. 6.

### A.2 Video

The Github repository includes image completion animations where the known and unknown pixels change dynamically, showcasing the versatility and robustness of the DRMM.

### A.3 Sampling Using a Gaussian Prior

Fig. 10 shows examples of applying Gaussian priors to a DRMM with three layers and 16 components per layer, trained with 2D Swiss roll data. Gaussian priors were discussed in Sec. 3.6 but not utilized in any of the experiments of Sec. 4.

An example of a real-life application that could utilize a Gaussian prior is movement synthesis in physically based computer animation: One could train a DRMM with state and action trajectories of a physically simulated agent. The model could then be queried for action sequences that allow reaching one or more goal states. If the agent is actuated with joint torques, a zero-mean Gaussian prior for actions would allow prioritizing energy conserving movements.



Figure 9: Visualizing the effect of the encoder-decoder skip-connections: Without the skip-connections, the samples are sometimes clearly from an incorrect MNIST class.

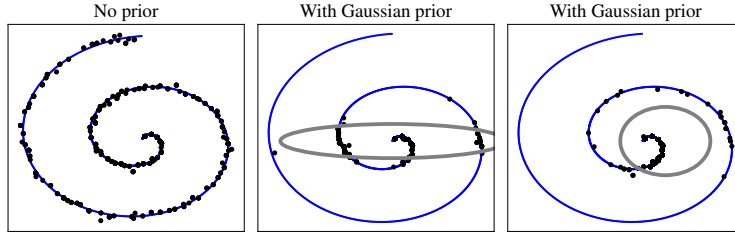


Figure 10: Examples of applying a Gaussian prior in sampling a DRMM trained with 2D Swiss roll data. The gray ellipses depict the area within two standard deviations of the prior Gaussian.

## B Sampling Bias

We make no formal claims of unbiasedness. Empirically, the histograms in Fig. 11 provide a good match with the reference data, and the approximation becomes more accurate with a deeper model. Similar to Fig. 1, one can observe the number of density modes modeled growing exponentially with depth, at least initially: The 1 and 2 layer models yields  $4^1$  and  $4^2$  modes, respectively. The visualization is not detailed enough for a precise analysis of the deeper models.

The backward sampling is bound to have some bias, however, as the independence assumption of the latent variables is at best only approximately valid. This is visualized in Fig. 12. Analyzing and correcting backward sampling bias is a topic for future work, although our image completion results demonstrate the usefulness of the backward sampling even without bias correction. We hypothesize that one may tackle the bias by adding a reconstruction loss that drives the backward pass memberships to match the forward pass ones.

## C Implementation details

### C.1 Training Schedule

As outlined in Sec. 3.5, we start with E-step  $\rho = 0$  and gradually increase it during training. More specifically, we use the following schedule in all our experiments:

$$\rho = \rho_{\text{final}}(0.5 + 0.5 \tanh(20(i - 0.5))), \quad (5)$$

where  $\rho_{\text{final}}$  is the value at the end of training, and  $i$  equals current training iteration divided by the total training iterations. We anneal the learning rate  $\beta$  quadratically after half of the training iterations have elapsed:

$$\beta = \beta_0 \min(1, (2 - 2i)^2), \quad (6)$$

where  $\beta_0$  is the initial learning rate.

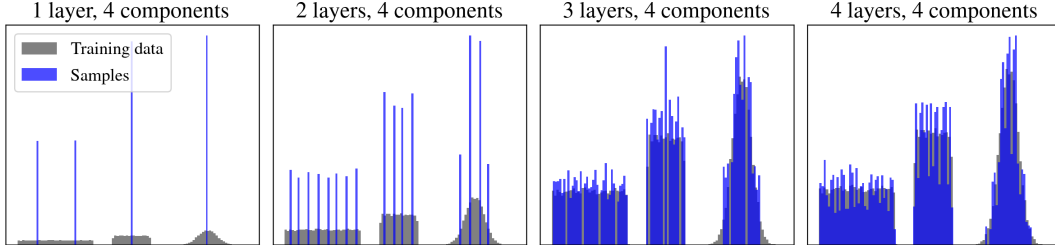


Figure 11: Histograms of training data and DRMM samples, using forward sampling and different model depths. Sample diversity and histogram accuracy increase with depth.

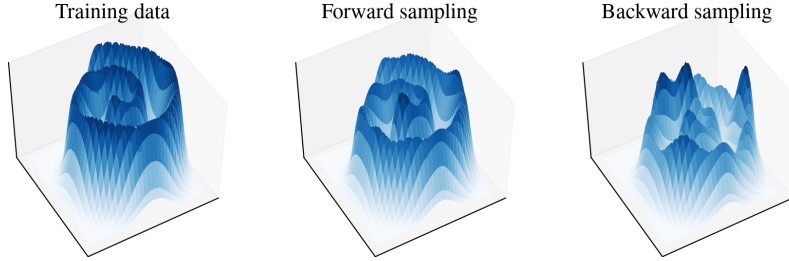


Figure 12: Gaussian kernel density estimates of 2D Swiss roll training data and DRMM samples, using both forward and backward sampling. The model has 4 layers, 16 components per layer. Both sampling methods distribute samples to correct areas, but the backward sampling does this less evenly.

## C.2 Gradient Stopping

We designed the DRMM for layer-wise training. However, we found that training is faster by training multiple layers in parallel, using the sum of layer losses as the total loss and gradient stops at layer inputs to prevent the losses from interacting. This means that later layers are chasing a moving target as earlier layers adapt, but the regularizations we apply appear adequate enough to handle that. Removing the gradient stops makes the training get stuck in a poor local optimum.

We also tried first training with gradient stops and removing the stops towards the end of training. Based on visualizations like Fig. 3, this can lead to the component means better fitting the residuals, but we have not (so far) observed a clear improvement in sample quality.

We train all the other models in a single run with the gradient stops, but in the image completion tests, this appears to result in reduced sample diversity. Thus, we train the image models in stages, one stage for each resolution level of the image patch modeling hierarchy. During each stage, E-step  $\rho$  and learning rate behave as described above.

## C.3 Training Time

We use 20k training iterations for the 2D plots, 100k iterations for IK, and 50k for the quantitative results in Fig. 7. In image completion, we train the patch DRMM blocks of each resolution level for 100k iterations and the final global DRMM block for 200k iterations. All 2D data tests were done on a laptop with a 4-core CPU and a NVIDIA 1060GTX GPU. The rest of the models were initially developed and tested on the laptop and later also deployed on Aalto University’s Triton computing cluster with NVIDIA P100 and V100 GPUs.

The approximate training times for the IK, MNIST, Quick! Draw, and CelebA networks are 1h, 3h, 12h, and 24h, respectively, using single-GPU jobs. The multiple training runs required for generating Fig. 7 take approximately half a day. According our system logs, the total GPU time used for the project is 80 days, including both finished and failed or terminated runs, and excluding the development laptop for which we do not have the data.



## C.4 Variable Masks

Conditioning samples on known variables can be implemented using the equality constraints of type  $\mathbf{a}^\top \mathbf{x} + b = 0$  discussed in Sec. 3.6. However, a more simple implementation is also possible. As explained in Sec. 3.1, the contributions of input variables combine additively in the log-membership probability computation. Thus, one can simply only perform the summation over the conditioning variables and leave out the unknown ones. In practice, we implement this using *masks* passed through the network with the data. The mask tensors are of the same shape as the input data, with ones for known variables and zeros for unknown ones. The masks are applied in Eq. (2) through elementwise multiplication.

By default, the masks for the sampled latent output variables of each layer are all ones; uncertainty is captured by the variance of the samples. However, with a small batch size, this can cause noticeable artefacts in backward sampling which uses batch-averaging to combine information from all the forward pass samples. As explained in Sec. 3.7, the batch-averaging is applied to the last layer’s forward pass outputs and the encoder-decoder skip-connections. A simple trick to reduce the artefacts is to use a zero latent output mask if all the input variables of a layer are unknown (*i.e.*, also have zero masks). Such a layer also uses zero skip-connection weight  $\alpha_{\text{skip}}$ . In image sampling, this means that a fully unknown image patch is only determined by the backward pass, whereas sampling a patch with some known pixels combines information from both the forward and backward passes.

## C.5 Image Completion Networks

As outlined in Sec. 4.2, the image completion networks consist of sequences of patch extraction and DRMM blocks. The residuals of block inputs are discarded at the block output, and the output only consists of the latent encoding produced by the block. The next block models patches of these encodings, as detailed in Table 1. The backward sampling inverts the patch extraction by overlap-averaging the patches.

Table 1: Network architectures used in Sec. 4.2

<i>Network</i>	<i>Input resolution</i>	<i>Operation</i>
MNIST	$28 \times 28$	Extract $3 \times 3$ patches with stride 2
	$14 \times 14$	Patch DRMM: 2 layers, 64 components per layer
	$14 \times 14$	Extract $3 \times 3$ patches with stride 2
	$7 \times 7$	Patch DRMM: 4 layers, 64 components per layer Global DRMM: 4 layers, 256 components per layer
Quick! Draw	$64 \times 64$	Extract $3 \times 3$ patches with stride 2
	$32 \times 32$	Patch DRMM: 3 layers, 32 components per layer
	$32 \times 32$	Extract $3 \times 3$ patches with stride 2
	$16 \times 16$	Patch DRMM: 4 layers, 64 components per layer
	$16 \times 16$	Extract $3 \times 3$ patches with stride 2
	$8 \times 8$	Patch DRMM: 5 layers, 128 components per layer
	$8 \times 8$	Extract $3 \times 3$ patches with stride 2
	$4 \times 4$	Patch DRMM: 6 layers, 256 components per layer Global DRMM: 10 layers, 256 components per layer
CelebA	$32 \times 32$	Extract $3 \times 3$ patches with stride 2
	$16 \times 16$	Patch DRMM: 4 layers, 64 components per layer
	$16 \times 16$	Extract $3 \times 3$ patches with stride 2
	$8 \times 8$	Patch DRMM: 6 layers, 128 components per layer
	$8 \times 8$	Extract $3 \times 3$ patches with stride 2
	$4 \times 4$	Patch DRMM: 8 layers, 256 components per layer Global DRMM: 10 layers, 256 components per layer

The weight sharing between the patch DRMMs is implemented using tensors of shape  $B \times W \times H \times C$  for each input stream, where  $B$  stands for batch size,  $W$  is width,  $H$  is height and  $C$  is the total number of pixel channels, *i.e.*, the previous block’s component count (latent variable PDF size) multiplied by the number of pixels in each patch. The memberships of Eq. (2) can then be computed for each of

the  $W \times H$  input patches using a single DRMM, implementing dot products as  $1 \times 1$  convolutions, and expressing the squared norm in Eq. (2) as three dot products:  $\|\mathbf{x} - \boldsymbol{\mu}\|^2 = \mathbf{x}^\top \mathbf{x} - 2\mathbf{x}^\top \boldsymbol{\mu} + \boldsymbol{\mu}^\top \boldsymbol{\mu}$ . As the forward pass outputs are averaged before the backward pass, the forward pass input batch is composed of copies of a single input image and its known variables mask.

We also noticed that since the image datasets we used were at least roughly normalized with respect to translation, we could get slightly better results by using per-pixel marginal component probabilities  $w_k$ , i.e., they were not shared by the patch DRMMs.

## C.6 Hyperparameters

No exhaustive search of hyperparameters was conducted. Hyperparameters were iterated manually over a few months of development. Most parameters were initially decided based on testing with simple 2D data (Fig. 1), with which training a network took less than a minute on a personal computer, allowing rapid iteration. Image network architectures and parameters were searched manually, testing different layer and component amounts, initial learning rates, and values 0, 0.1, 0.2, 0.5, 1.0 for  $\rho_{\text{final}}$ .

Table 2: Hyperparameters

<i>Parameter</i>	<i>Explanation</i>	<i>Value</i>
$\rho_{\text{final}}$	E-step $\rho$ at the end of training (App. C.1)	0.5 (image sampling), 1.0 (other)
$\beta_0$	Initial learning rate (App. C.1)	0.005 (2D tests and Fig. 7) 0.002 (other)
$\epsilon$	Categorical PDF smoothing coefficient (Sec. 3)	$10^{-8}$
$\alpha$	Regularization loss weight (Sec. 3.5)	0.01
$\alpha_t$	Image sampling truncation threshold (Sec. 4.2)	0.02
$\alpha_{\text{skip}}$	Encoder-decoder skip-connection weight (Sec. 3.7)	0.5

## C.7 Avoiding Cherry-picked Results

During development, results and figures were naturally regenerated multiple times. Cherry-picking was avoided by generating all results of a particular type in one go, *e.g.*, all image samples of a particular dataset, or all the different goal and constraint combinations in Fig. 5. The selection of test images was also kept the same throughout the project. Our image sampling figures use the first Quick! Draw and CelebA images as the test inputs, omitting them from training. For MNIST, we use the first test set images as inputs, and the model was trained on the training set.

## C.8 F1 Scores

The F1 score is the harmonic mean of precision and recall:  $F_1 = 2(\text{recall} \times \text{precision}) / (\text{recall} + \text{precision})$ . We add  $\epsilon$  to the denominator to handle zero precision and recall. We compute precision and recall using the method and code of Kynkäänniemi et al. [37]<sup>1</sup>, using 20k samples (or full dataset for smaller datasets) and batch size 10k.

To save computing resources, we did not average the F1 scores in Fig. 7 over multiple training runs. Nevertheless, the results should be reliable, as each plotted curve is already the result of multiple runs, one per plotted point, and if there was significant randomness, the curves would not behave as consistently as in observed in Fig. 7.

In creating Fig. 7, we trained and tested baseline GMMs with 64, 128, 256, 512, and 1024 components. We tested DRMM depths 1, 2, 3, 4, and for each depth, the amounts of components were selected to yield total parameter counts as close to the baseline as possible. Although the baseline could be stronger if full covariances were used, we chose the scalar covariance to allow implementing the baseline using our DRMM codebase, thus eliminating any confounding differences (training algorithm, other implementation details) in comparing against the baseline.

<sup>1</sup><https://github.com/kynkaat/improved-precision-and-recall-metric>

## C.9 Datasets

MNIST image data was used as is. The Quick! Draw data is in the form of point sequences describing drawing strokes. These were rasterized with antialiasing into  $64 \times 64$  pixel images. The CelebA images were cropped before scaling down to the training resolution to maintain enough detail for facial features such as eyes. The cropping removed 40 pixels from left and right, 30 pixels from top, and 50 pixels from the bottom. Due to constrained computing resources, we have not yet tried to model full-resolution CelebA images or other high-resolution image datasets.